Showcasing research from Professor Germino and Pereira laboratory, i3N/Physics Department, University of Aveiro, Portugal, and professor Therezio's laboratory, IF, UFMT, Brazil.
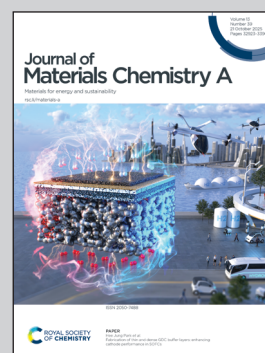
Can chelatogenic molecules enhance the stability of air-processed MAPbI$_3$ perovskite solar cells? A case study of salophen

Our study investigates salophen molecules for enhancing stability of air-processed MAPbI$_3$ PSC. Incorporating salophen during the antisolvent step improved crystallization, defect passivation, charge-carrier transport and hydrophobic surface formation. These modification enables to achieve PCE over 18%, demonstrating a promising strategy for improving long-term stability of PSCs.

Image reproduced by permission of José Carlos Germino from *J. Mater. Chem. A*, 2025, **13**, 33175.

Image created using Google Gemini.

ROYAL SOCIETY OF **CHEMISTRY**

rsc.li/materials-a

Can chelatogenic molecules enhance the stability of air-processed MAPbI₃ perovskite solar cells? A case study of salophen

Andreia de Morais, [ab] Francisco Nascimento Silva, [c] Higor Ribeiro Ormonde, [c] Romildo Jerônimo Ramos, [c] Emmanuel S. Moraes, [ad] B. M. G. Melo, [d] Luiz Pereira, [d] Ana Flávia Nogueira, [a] Jilian Nei de Freitas, [b] José Carlos Germino *[d] and Eralci Moreira Therézio *[c]

Perovskite solar cells have attracted attention in recent years due to their low-cost fabrication and high-power conversion efficiency. For practical applications, however, long-term stability is still a problem. The perovskite layer degrades when exposed to moisture, oxygen, temperature and UV radiation. One strategy to overcome this limitation is the modification/passivation of the perovskite layer. The use of chelatogenic molecules is an effective method because their functional groups can coordinate with the metallic center (Pb^{2+}) of the perovskite, thereby enhancing its structural stability. Herein, we demonstrate the effect of incorporating N,N'-bis(salicylidene)-o-phenylenediamin (salophen) molecules (a Schiff base) on methylammonium lead iodide perovskite ($MAPbI_3$) thin films. Salophen was dissolved in ethyl acetate solvent at five different concentrations and spin-coated onto $MAPbI_3$ during the antisolvent step under ambient conditions (room temperature; relative humidity over 50%). X-ray diffractograms reveal that the addition of salophen molecules on the top of the $MAPbI_3$ films induces better crystallization of the perovskite α-phase, eliminating the residual amount of PbI_2, which simultaneously creates a hydrophobic protective surface. Steady-state photophysical characterization shows that the salophen molecules did not significantly change the optical properties of the $MAPbI_3$ films. Nonetheless, time-resolved photoluminescence decays clearly exhibit a charge-carrier extraction pathway through the salophen passivation of $MAPbI_3$ defects while enhancing thin film organization, a behaviour proven with surface electron microscopy images. Device efficiencies reached values higher than 18%, along with gains in stability.

1 Introduction

Since Miyasaka and his collaborators' pioneering work, lead halide perovskites (LHPs) have been one of the most attractive emergent materials for photovoltaic (PV) technology applications.[1] Perovskite solar cells (PSCs) have shown an incredible power conversion efficiency (PCE) enhancement over time, from 3.9% in 2009[2] to the actual record of 27%.[3] This fast increase in the PSC efficiency is directly related to some intrinsic features of LHP materials: (a) an extended energy absorption band between the near-infrared and visible spectrum;[4] (b) tolerance to electronic defects;[5,6] (c) a low exciton dissociation energetic barrier

in the order of room-temperature ($k_BT \sim 25$ meV);[7,8] (d) a high absorption cross-section (direct band gap);[9] (e) ambipolar electrical transport (intrinsic semiconducting material), with high electron and hole charge-carrier mobilities;[10,11] (f) long charge-carrier lifetimes[12] and (g) large exciton diffusion lengths ($L_D > 1$ μm).[13] These combined characteristics make LHPs an excellent emergent material for PV devices, particularly in niche applications.

Despite the great advantages that LHPs have in contrast to other materials for photovoltaic purposes, they still have some drawbacks. Among the several issues reported in published works, we point out that stability problems (which are undoubtedly one of the most important) remain under discussion in the scientific field and not yet fully explained, such as strong sensitivity to the processing device conditions (environment temperature, water on the precursor solvent, spin-coating randomness and parameter fluctuations, type of antisolvent and their drop conditions, blade coating solvent evaporation time, among others);[14–16] thermal instability;[17–19] water and oxygen sensitivity;[20,21] structural mismatching between each

a Institute of Chemistry, University of Campinas, Campinas, SP, 13083-970, Brazil

b Center for Information Technology Renato Archer–CTI, Campinas, Brazil

c Institute of Physics, Federal University of Mato Grosso, Cuiabá, MT, 78060-900, Brazil. E-mail: therezio@fisica.ufmt.br

d Department of Physics, i3N–Institute for Nanostructures, Nanomodelling and Nanofabrication, University of Aveiro, Aveiro, 3810-193, Portugal. E-mail: germino@ua.pt

This journal is © The Royal Society of Chemistry 2025

J. Mater. Chem. A, 2025, **13**, 33175–33187 | 33175

PSC layer; deep-trap formation in the grain boundaries (*i.e.* interstitial I_3^- and Br_3^- and Pb^0 cluster species as hole traps and halide vacancies (V_X^-) as electron traps),[22–26] and more recently discrepancies between indoor and outdoor tests. Considering all these features, processing perovskite thin films without a controllable atmosphere, *i.e.*, outside nitrogen or argon-filled conditions, remains a real challenge for upscaling PSC technology and even for some feasible marked applications.[27–31]

In this sense, solvent engineering protocols, antisolvents, which can eliminate water molecules from the perovskite thin-film, additives in LHP's precursor solution, and surface treatment, are strategies that have been pointed out and adopted by the research community to overcome these issues under normal environmental processing conditions.[32–34] Nogueira and collaborators[35] proposed the use of ethyl acetate (EA) as an antisolvent and, simultaneously, incorporated poly(ethylene oxide) copolymers (PEO-CPs) in the methylammonium lead(II) triiodide (MAPbI$_3$) perovskite, processing it under air conditioning (rh ~50%). The EA antisolvent enables the elimination of water molecules from perovskite precursor solutions and those contained in the atmosphere; simultaneously, PEO-CPs increase stability according to the ISOS-D-1 protocol although at a cost of lower efficiencies. The stability enhancement was attributed to the formation of hydrogen bonds between methylammonium and oxygen atoms present in the PEO-CP main chain and possible halide vacancy defect passivation.

However, organic chelates play an important role in the V_X^- defect passivation. They can simultaneously create a hydrophobic molecular layer that protects the perovskite from water and oxygen molecules, inhibiting ionic migration and Pb(II) leaching, as reported by Chen et al.,[36] using an ethylenediamine tetraacetate (EDTA^{4-}) ligand in a post-passivation approach (after perovskite film formation). They also reported an improvement in PSC stability under ambient-air conditions, along with a decrease in lead(II) leakage. Yang and co-authors[37] have shown that EDTA chelate can decrease SnO$_2$ interface mismatching with the perovskite active layer, which improves the efficiency and stability of the photovoltaic device. However, these kinds of organic chelates directly affect the charge-carrier transport features of the perovskite layer owing to their dielectric behaviour, which can influence the solar-to-electricity conversion performance. In this sense, employing a semiconducting organic chelate appears to be an excellent alternative for defect passivation and waterproof protection, without impairing the electrical and optical characteristics of the perovskite films. Other organic semiconducting chelates were previously employed for enhancing the performance and stability of PSC devices.[38–43] Li et al. reported the functionalization of a multi cation mixed-halide perovskite with ferrocenyl-bis-thiophene-2-carboxylate molecules, which achieved PCE over 25%, maintaining stability >98% along a 1500 h test.[38]

N,N'-bis(salicylidene)-*o*-phenylenediamine (salophen) is a kind of N$_2$O$_2$-donor Schiff Base molecule, which has proven to be an excellent chelate ligand for most transition and non-transition metal cations, forming a coordination compound ([M(salophen)]).[44] These metal complexes can exhibit a wide range of applications, where sensing,[45] catalysis,[46] non-linear optics (NLOs),[47] medicine[48] and optoelectronics[49] might be highlighted. Our research team has been contributing to the state-of-the-art M(salophen) compounds during recent years in the field of NLOs[50–52] and optoelectronic[53–58] applications, highlighting that simple and low-cost chemical changes in the salophen ligand framework lead to considerable response changes and enhancements. Barboza et al.[59] showed that small chemical changes in the ligand structure create a complete change in the M(salophen)'s electronic structure and photophysical properties in solution and solid-state. Germino et al.[60] and Duarte et al.[54] proved that the insertion of specific chemical groups, particularly benzophenone and benzothiazole, into the salophen framework enhances the optoelectronic features of their Zn(II) coordination compounds when applied as an active layer in all solution-processed organic light-emitting diodes (OLEDs). The same chemical modifications led Vivas and co-authors[52] to observe an enhancement of NLO properties, in terms of incoherent second-order non-linear optical response in [Zn(salophen)] compounds. Inspired by Yersin et al.[61] and Zhang et al.[49] works, Germino et al.[62] were able to synthesize and fully characterize (structurally and optically) phosphorescent [Pt(II)salophen's)] coordination compounds using the same ligand modification concept and successfully apply them as guest (red-emitter) for all-solution-processed high-efficiency white OLEDs (WOLEDs), achieving EQE values above 15%. It is very important to highlight that salophen ligands and their metal complexes can enhance the charge-carrier transport in devices,[54,57] which may be a key point when this molecule passivates structural defects between lead-halide perovskite grain boundaries.

Considering (i) the importance of developing feasible air-processing protocols for obtaining a useful PSC, (ii) the defects control and stability against room humidity by chelatogenic organic compounds, and (iii) the environmental impact of Pb(II) cation leaking, herein, we demonstrate the use of salophen chelate molecules to improve the stability and figures of merit on MAPbI$_3$-based PSCs processed under ambient conditions. We demonstrate that salophen chelate is an effective semiconducting molecular system for surface and grain boundary interface defect passivation of MAPbI$_3$ thin films. This approach can improve the structural, optical, and electrical characteristics and stability of PSCs, creating a better interface between the active layer and the HTM layer. Consequently, we obtain highly stable and efficient PSCs under ambient conditions, shining light on the usage of semiconductive chelate molecules on the perovskites for optoelectronic applications.

2 Experimental section

2.1 Materials

Fluorine-doped tin oxide (FTO)-coated glass substrates (TEC7 Glass Plates, 300 mm × 300 mm × 2.2 mm, ~7 Ω sq^{-1}), methylammonium iodide (MAI, ≥99.99%), 30 NR-D transparent TiO$_2$ paste, and tris(2-(1*H*-pyrazol-1-yl)-4 *tert*-butylpyridine) cobalt(III)tri[bis(trifluoromethane)sulfonimide] (FK209 Co(III) TFSI) were purchased from GreatCell Solar Materials LTD (Queanbeyan, Australia). Titanium diisopropoxide

33176 | *J. Mater. Chem. A*, 2025, **13**, 33175–33187

This journal is © The Royal Society of Chemistry 2025

bis(acetylacetonate) (75 wt% in isopropanol, 98%), ethanol (anhydrous, ≥99.5%), chlorobenzene (anhydrous, 99.8%), N,N-dimethylformamide (DMF, anhydrous, 99.8%), dimethyl sulfoxide (DMSO, anhydrous, ≥99.9%), acetonitrile (ACN, anhydrous, 99.8%), 4-terc-butylpyridine (TBP, 98%), lithium bis(trifluoromethanesulfonyl)imide (LiTFSI, 99.95%), 1,2-phenylenediamine (99.5%), salicylaldehyde (98%), zinc (Zn) powder (98%), and hydrochloric acid (HCl, 36.5-38.0%) were purchased from Sigma-Aldrich. Lead iodide (PbI$_2$, 99,99%) was acquired from Tokyo Chemical Industry (TCI), America Inc., and 2,2′,7,7′-tetrakis(N,N-di-p-methoxyphenyl-amine)9,9′-spiro-bifluorene (Spiro-OMeTAD) was purchased from Xi'an Polymer Light Technology Corp.

2.2 Synthesis of salophen

The Schiff base was synthesized following the protocol described by Barboza et al.,[59] with some modifications. Initially, 1,2-phenylenediamine (1 mmol) was diluted in ethanol (25 mL) under constant stirring. After 5 min, salicylaldehyde (2 mmol) was added dropwise into the reaction medium under constant stirring until the formation of salophen crystals. The final product was vacuum filtered, washed with ethanol, and air-dried overnight at 25 °C. The synthesis scheme for salophen is shown in Fig. 1.

2.3 Substrate preparation

FTO substrates (2.5 cm × 1.5 cm) were patterned using Zn powder and HCl (4.0 mol L^{-1}) for chemical etching. Polyimide (Kapton®) tape was used to protect the FTO surface from corrosion. Patterned FTO substrates were cleaned in an ultrasonic bath with aqueous Hellmanex® (2% v/v) solution for 25 min, followed by deionized water, acetone, and isopropanol for 15 min each. After drying in nitrogen (N$_2$) gas flow, the FTO substrates were treated in a UV-ozone chamber for 30 min at room temperature.

2.4 PSC assembly

PSCs with architecture FTO-glass|c-TiO$_2$|meso-TiO$_2$|MAPbI$_3$ or MAPbI$_3$: salophen|Spiro-OMeTAD|Au (active area of 0.16 cm^2) were fabricated under normal ambient conditions (outside the glovebox), except for the Spiro-OMeTAD and Au layers. First, the patterned FTO substrates were transferred to a hot plate and quickly heated up to 450 °C. In sequence, a compact TiO$_2$ layer

(c-TiO$_2$) (ETL) was deposited onto the FTO substrates by aerosol spray pyrolysis, from a sprayed solution of 400 μL of acetylacetone and 600 μL of titanium diisopropoxide bis(acetylacetonate) in 9 mL of ethanol, using pure oxygen gas as a carrying gas. The c-TiO$_2$ films were annealed at 450 °C for 30 min. To prepare the mesoporous TiO$_2$ layer (meso-TiO$_2$), 30 N-RD Dyesol TiO$_2$ paste was diluted in ethanol (150 mg mL^{-1}).[35] The TiO$_2$ dispersion was maintained under vigorous stirring overnight prior to use. The meso-TiO$_2$ dispersion (ETL) (80 μL) was deposited by spin-coating at 4000 rpm for 30 s (2000 rpm s^{-1}); then, the films were sintered in multiple temperature steps as reported by Saliba et al.[63]

The perovskite active layer of MAPbI$_3$ was prepared by applying a one-step method.[35] First, the perovskite stock solution was prepared by dissolving 1290 mg of PbI$_2$ and 444 mg of MAI in 2 mL of a solvent mixture of DMF and DMSO (4 : 1 v/v). An aliquot of the MAPbI$_3$ solution (60 μL) was deposited by spin-coating at 1000 rpm for 10 s (200 rpm s^{-1}), followed by 4000 rpm for 20 s (2000 rpm s^{-1}), and 200 μL of ethyl acetate (antisolvent) was spin cast onto the MAPbI$_3$ film in the final 10 s. Different salophen solutions in ethyl acetate (0.05 to 5.0 mmol L^{-1}) were also used as antisolvents. Finally, the MAPbI$_3$ and MAPbI$_3$:-salophen films were thermally annealed at 100 °C for 30 min. The Spiro-OMeTAD layer (HTL) was prepared inside the glovebox as follows: 100 mg of Spiro-OMeTAD was dissolved in 1 mL of chlorobenzene and stirred at room temperature for 20 min. The additives TBP (36 μL), LiFTSI (20 μL, 1.8 mol L^{-1} in acetonitrile) and FK209 (8 μL, 0.25 mol L^{-1} in acetonitrile) were added to the Spiro-OMeTAD solution and remained upon stirring for 10 min. An aliquot of the Spiro-OMeTAD solution (50 μL) was deposited on the MAPbI$_3$ and MAPbI$_3$: salophen films by spin-casting at 4000 rpm for 20 s. The films were removed from the glovebox and stored overnight in a desiccator to allow for the oxidation process of the Spiro-OMeTAD layer. Finally, inside the glovebox, Au electrodes with a thickness of 80 nm were deposited by thermal evaporation in a high vacuum chamber (∼5 × 10^{-6} mbar), at a rate of 0.1 A s^{-1} (4 nm) and 1.0 A s^{-1} (76 nm), through a shadow mask. PSC architecture, salophen molecular structure, assembled device and energy level of each PSC component are shown in Fig. 2.

2.5 Electrical characterization of PSCs

The current density–voltage (J–V) curves were acquired upon white light illumination (100 mW cm^{-2}, AM 1.5 G) with a class
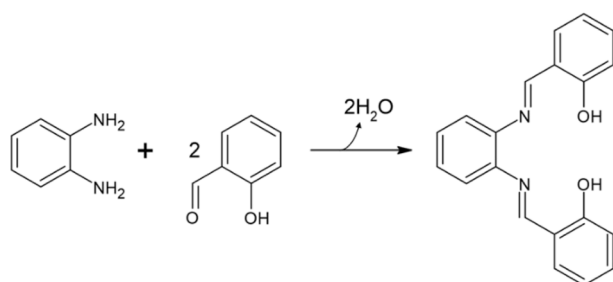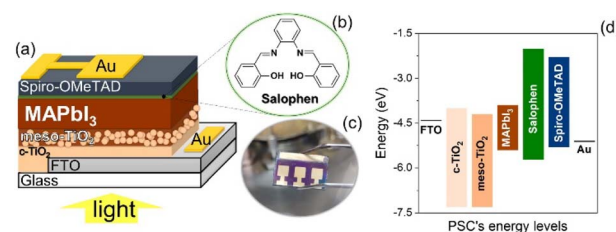

Fig. 1 Synthesis scheme of salophen.

Fig. 2 Perovskite solar cell architecture (a), salophen molecular structure (b), device photography (c) and energy levels below vacuum diagram (d).

This journal is © The Royal Society of Chemistry 2025

J. Mater. Chem. A, 2025, **13**, 33175–33187 | **33177**

AAA Solar Simulator (HAL-320, Asahi Spectra Co., Ltd) using a Keithley 2400 SourceMeter. The simulator was calibrated using a silicon reference solar cell with a KG5 filter. Stability tests were carried out according to ISOS-D-1 protocol.[64] These tests were performed under ambient conditions at room temperature, relative humidity and in the dark, without any encapsulation. The photovoltaic response from the PSCs was monitored for 720 h.

2.6 Characterization of MAPbI$_3$ and MAPbI$_3$: salophen films

2.6.1 Structural characterization. X-ray diffraction (XRD) patterns were acquired using a PANalytical AERIS diffractometer, Cu Kα radiation source (1.54056 eV), operating at 40 kV and 15 mA. Diffractograms were collected with 0.003° steps, 0.5 seconds per step acquisition time and an angular range from 10° to 60° in 2θ.

2.6.2 Morphological characterization. Scanning electron microscopy (SEM) images of the FTO|c-TiO$_2$|mp-TiO$_2$|MAPbI$_3$ and MAPbI$_3$: salophen films were obtained on a Field Emission Gun Scanning Electron Microscope (FEG-SEM) (MIRA 3 XMU model, TESCAN, Brno, Czech Republic), with electron energies of 10 kV, in high vacuum. Before analysis, all the samples were coated with a thin Au layer using a standard sputtering technique.

2.6.3 Optical characterization. UV-vis absorption spectra of the MAPbI$_3$ (control) and MAPbI$_3$: salophen films were acquired using an Agilent Cary 60 UV-vis spectrophotometer. A glass substrate was used as a baseline for all the spectra. Photoluminescence (PL) spectra were performed using an Ocean Optics QE Pro scientific grade spectrometer with an LED ($L_{exc} = 365$ nm) as the excitation light source.

Time-resolved photoluminescence (TrPL) decays of the MAPbI$_3$ and MAPbI$_3$: salophen thin films were obtained from time-correlated single-photon counting (TCSPC) in an Edinburg Analytical Instruments FL 900 spectrofluorometer with an MCP-PMT (Hamamatsu R3809U-50; 50 ps) and a PicoQuant LDH-D-C-440 pulsed diode laser, operating at $\lambda_{exc} = 440$ nm (bandwidth of 5 nm, pulsewidth = 80 ps; $F = 9.7$ nJ cm^{-2}). The emission signals were collected at the maximum emission wavelength of each sample on a time scale of 2 μs. The instrument response was recorded using a Ludox sample.

3 Results and discussion

3.1 Characterization of MAPbI$_3$ and MAPbI$_3$: salophen films

The structural, optical and morphological properties of the pristine MAPbI$_3$ film (control) and MAPbI$_3$: salophen (from 0.05 to 5.0 mmol L^{-1}) films were investigated. Fig. 3 shows the room temperature diffractograms and Rietveld refinement for the samples. In addition to the perovskite MAPbI$_3$ phase (ICDD pattern 01-085-5508), the films exhibited the formation of PbI$_2$ (ICDD pattern 00-007-0235). The results obtained from the Rietveld refinement (Table 1 and Fig. S1, SI) indicate the formation of the tetragonal crystalline phase (I4/*mcm* space group) in the MAPbI$_3$ films. The main diffraction peaks of MAPbI$_3$ localized at 2θ = 14.0°, 19.9°, 24.3°, 28.2°, 31.7°, 34.8°,
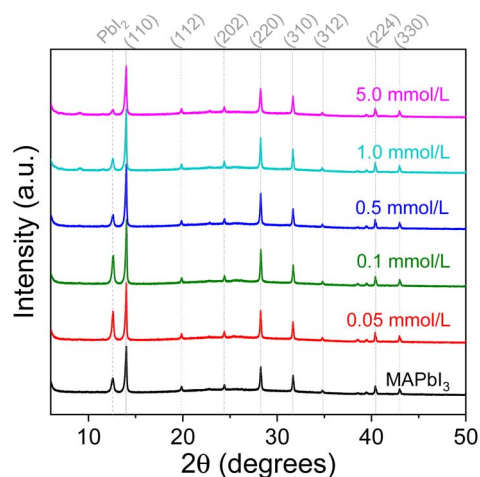

Fig. 3 XRD patterns of the pristine MAPbI$_3$ (control) and MAPbI$_3$: salophen (0.05 to 5.0 mmol L^{-1}) films.

40.4°, and 43.0° can be attributed to the crystalline planes (110), (112), (202), (220), (310), (312), (224), and (330), respectively. The results indicate the formation of the tetragonal crystalline phase (14/*mcm* space group) in the MAPbI$_3$ films.[65]
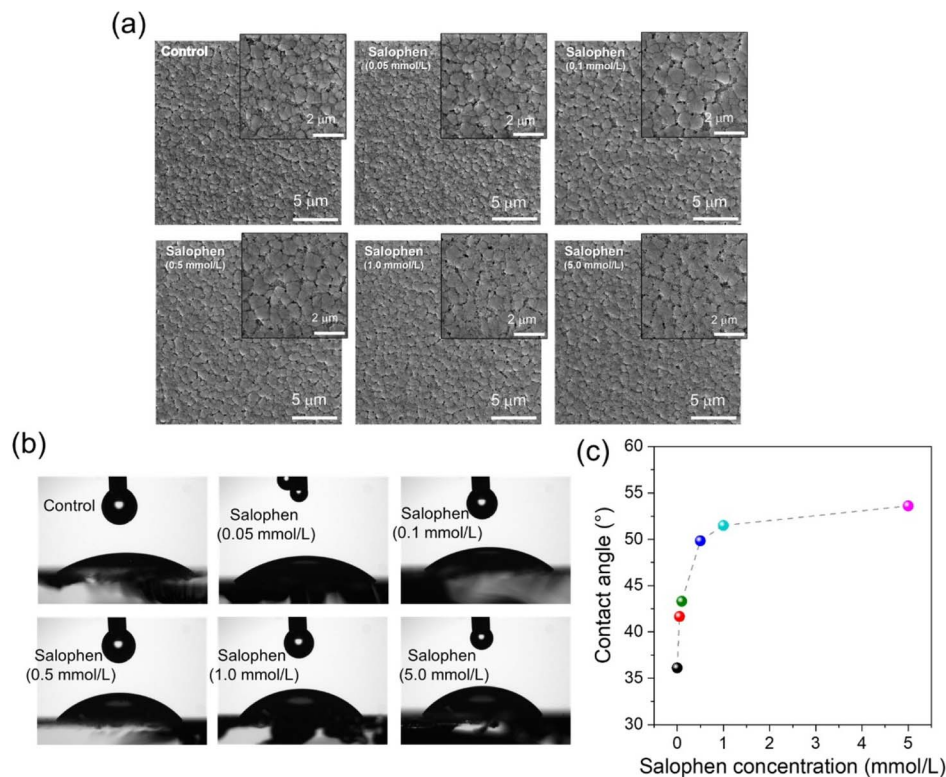
Overall, the crystallization and orientation of the MAPbI$_3$ films were not significantly affected by surface modification with salophen. All films exhibit a preferred orientation along the (110) and (220) crystalline planes. The diffraction peak centred at 2$\theta = 12.6$° refers to the (100) crystalline plane of PbI$_2$, indicating an incomplete conversion of the precursors into perovskite.[66] The XRD patterns also show a reduction in the intensity of the PbI$_2$ peak with increasing salophen concentration in MAPbI$_3$ films, except for low salophen concentrations (0.05 and 0.1 mmol L^{-1}). The overall data are presented in Table 1. As shown in the table, for the MAPbI$_3$ film with salophen at a concentration of 5.0 mmol L^{-1}, the wt% of the PbI$_2$ phase was reduced to 3.34%. These results indicate that adding salophen molecules promotes a more effective conversion of the perovskite (MAPbI$_3$) to the black-phase (α-phase). This phase is particularly desirable for photovoltaic applications owing to its superior electronic properties.

FEG-SEM images (see Fig. 4a) were obtained to investigate the surface morphology of the pristine MAPbI$_3$ and MAPbI$_3$: salophen films. All the films show good coverage of the TiO$_2$

Table 1 Rietveld refinement values obtained from the XRD patterns of the pristine MAPbI$_3$ (control) and MAPbI$_3$: salophen (0.05 to 5.0 mmol L^{-1}) films are shown in Fig. S1 (SI)

Sample	MAPbI$_3$ α-phase (wt%)	PbI$_2$ (wt%)	R_{exp}	R_p	R_{wp}	χ^2
MAPbI$_3$	88.41	11.59	3.39	3.69	5.16	1.52
0.05 mmol L^{-1}	83.28	16.72	3.23	4.05	5.71	1.77
0.1 mmol L^{-1}	83.44	16.56	3.21	4.41	6.10	1.90
0.5 mmol L^{-1}	93.61	6.39	3.25	3.89	5.28	1.63
1.0 mmol L^{-1}	92.58	7.42	3.39	4.25	6.10	1.80
5.0 mmol L^{-1}	96.66	3.34	3.41	3.89	5.46	1.60

33178 | *J. Mater. Chem. A*, 2025, **13**, 33175–33187

This journal is © The Royal Society of Chemistry 2025

Fig. 4 (a) FEG-SEM images of FTO|c-TiO$_2$|meso-TiO$_2$|MAPbI$_3$ (control) and FTO|c-TiO$_2$|meso-TiO$_2$|MAPbI$_3$: salophen (from 0.05 to 5.0 mmol L^{-1}) samples. Scale bars indicate 5 μm in FEG-SEM images. FEG-SEM images are also shown in the insets, with scale bars representing 2 μm. (b) Contact angle images and (c) contact angle as a function of salophen concentration.

ETL. The morphology of the pristine MAPbI$_3$ film reveals grains with varying sizes between 0.2 and 1.2 μm. The addition of salophen ($\geq$0.1 mmol L^{-1}) over the MAPbI$_3$ layer promoted an improvement in the uniformity of grain sizes (0.9–1.2 μm). However, at higher concentrations of the salophen ($\geq$1.0 mmol L^{-1}), FEG-SEM images reveal the formation of needle-like structures on the surface and between grain boundaries. To better understand the influence of the salophen molecules in the MAPbI$_3$ film formation, morphology and structure, we collected cross-section images for the control and the high-concentrated salophen-modified film (5 mmol L^{-1}) (see Fig. S2, SI). In fact, as observed in the FEG-SEM top-view images, salophen molecules can enhance perovskite grain contact, thereby diminishing grain boundary defects. This effect can improve perovskite stability against ambient conditions, as discussed in Subsection 3.2.

Water contact angle measurements were performed to evaluate water resistance in MAPbI$_3$ films after salophen modification. Fig. 4b and c shows the contact angle images of water droplets on the FTO/MAPbI$_3$ and MAPbI$_3$: salophen (0.05 to 5.0 mmol L^{-1}) surfaces, and contact angle variation with different salophen concentrations. The water contact angle for the pristine MAPbI$_3$ film (control) was 36.1°, which increased to 53.6° for the MAPbI$_3$: salophen (5.0 mmol L^{-1}) film. The MAPbI$_3$ films with salophen at concentrations of 0.05 mmol L^{-1}, 0.1 mmol L^{-1}, 0.5 mmol L^{-1}, and 1.0 mmol L^{-1} showed a progressive increase in the contact angle, with values of 41.7°,

43.3°, 49.8°, and 51.5°, respectively. It can be achieved that the water contact angle increases with salophen concentration owing to the hydrophobic nature of this Schiff base. This enhancement of the hydrophobicity of the modified MAPbI$_3$ surface can contribute to increasing the stability of the corresponding PSCs.

Fig. 5a–c shows the steady-state, time-resolved PL (TrPL) decays and the charge-carrier recombination dynamics for the MAPbI$_3$ and MAPbI$_3$: salophen films.

Any addition of the salophen compound did not considerably disturb the electronic absorption spectrum of MAPbI$_3$, which maintained its optical bandgap energy (Fig. 5a). The same behaviour was observed in the steady-state PL spectra of the samples (inset Fig. 5a). Conversely, the TrPL measurements (λ_{exc} = 445 nm; λ_{PL} = 780 nm) reveal that adding salophen chelate molecules to MAPbI$_3$ completely changes the charge-carrier dynamics of the films. We clearly observe in Fig. 5b that the addition of the salophen molecules decreases the charge-carrier lifetime of the perovskite, suggesting a better charge-carrier extraction from the MAPbI$_3$ layer. The charge-carrier lifetime starts to increase from concentrations above 0.05 mmol L^{-1} of the chelate. To better understand the charge carrier transport and recombination processes, and the effect of the salophen molecules added to MAPbI$_3$ films, we adjust each TrPL decay according to the third-order recombination dynamics, following differential eqn (1):[67,68]
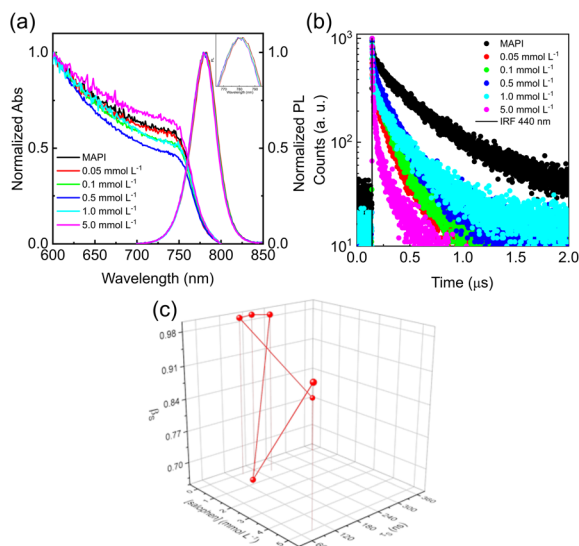
Fig. 5 (a) Electronic absorption and steady-state PL spectra, (b) TrPL decays (λ_{exc} = 445 nm and λ_{PL} = 780 nm), and (c) obtained charge-carrier lifetimes and disorder parameters as a function of the salophen concentration for MAPbI$_3$ and MAPbI$_3$: salophen (0.05 to 5.0 mmol L^{-1}) films.

$$\frac{\mathrm{d}n(t)}{\mathrm{d}t} = -k_3 n^3 - k_2 n^2 - k_1 n, \tag{1}$$

where n is the charge carrier density, t is the time, k_1 is the monomolecular trap-assisted (first-order), k_2 is the band-to-band (second-order), and k_3 is the complex Auger (third-order) recombination rate. However, high-order charge carrier recombination processes can be neglected at low fluence regimes (F = 9.7 nJ cm^{-2}), as time-correlated single-photon counting (TCSPC) experiments were performed. Thus, in this regime, TrPL decays should exhibit monoexponential behaviour. Nonetheless, owing to spin-coating film formation, a high disorder level and random crystal size may lead to complex emission decay, which was adjusted using a stretched exponential decay model (eqn (2)):[68]

$$I(t) = I_0 \mathrm{e}^{-\left(\frac{t}{\tau_S}\right)^{\beta_S}}, \tag{2}$$

where $I(t)$ is the time-dependent intensity (directly proportional to the $n(t)$), I_0 is the intensity at the time "zero", τ_S is the charge carrier lifetime, and β_S is the stretching factor, also known as the disorder parameter, which was set as a boundary condition as $0.5 < \beta_S \leq 1$.

By applying this model to adjust the TrPL decays, we observe that the addition of the salophen chelate molecules on the top of the MAPbI$_3$ films considerably reduces the charge carrier lifetimes, respecting the following decrescent order: $\tau_{(MAPbI_3)}$ = 358 ns > $\tau_{(0.5\ mmol\ L^{-1})}$ = 207 ns > $\tau_{(0.1\ mmol\ L^{-1})}$ = 177 ns > $\tau_{(0.05\ mmol\ L^{-1})}$ = 147 > $\tau_{(1.0\ mmol\ L^{-1})}$ = 131 ns > $\tau_{(5.0\ mmol\ L^{-1})}$ = 87 ns. Nonetheless, the disorder parameter increases consistently with the addition of the salophen, from 0.78 for the neat MAPbI$_3$ film to 0.99 for the lowest chelate concentration, 1.0 for 0.1 and 0.5 mmol L^{-1}, and finally, decreases for the highly

concentrated film (β_S = 0.66 and 0.93 for 1.0 and 5.0 mol L^{-1}, respectively). The observed values lead us to conclude that the salophen molecules passivate MAPbI$_3$ defects and, simultaneously, contribute to a better crystallization process in the film formation, which agrees with the SEM microscopy images and XRD patterns. However, a high density of salophen molecules (>1.0 mmol L^{-1}) induces a worsening of the MAPbI$_3$ thin-film morphology, increasing the perovskite film defects, and then can negatively impact the figures of merit of the overall perovskite solar cells.

3.2 Perovskite solar cells

The effect of varying salophen concentrations in ethyl acetate (from 0.05 to 5.0 mmol L^{-1}) as an antisolvent on the MAPbI$_3$ layer can be further explored in PSC devices. To this end, we assembled PSCs with an n–i–p configuration: FTO-glass|c-TiO$_2$|meso-TiO$_2$|MAPbI$_3$ or MAPbI$_3$:salophen|Spiro-OMeTAD | Au. The J–V curves in the forward and backward scan directions, under illumination and in the dark, for the best-performing PSCs are shown in Fig. 6.

As depicted in Fig. 6, the best pristine PSC (control) reached 18.55% and 14.39% of power conversion efficiency (PCE) for backward and forward scans, respectively. We observed a slight decrease in the PCE values for the devices containing a MAPbI$_3$: salophen layer at low concentrations (up to 1.0 mmol L^{-1}), varying from 18.55% (control, without salophen) to 17.56% (with 1.0 mmol L^{-1} of salophen). At higher concentrations ($\geq$1.0 mmol L^{-1}), the PCE values decrease sharply to 14.36% using 5 mmol L^{-1} of salophen as an antisolvent on the perovskite layer. The device containing a salophen-modified MAPbI$_3$ layer at a concentration of 10 mmol L^{-1} of salophen in the antisolvent was also assembled and showed a lower PCE value (13.53%) (see Fig. S3, SI). The statistical distributions of the photovoltaic parameters for each salophen concentration (from 0.05 to 5.0 mmol L^{-1}) used as antisolvent are shown in
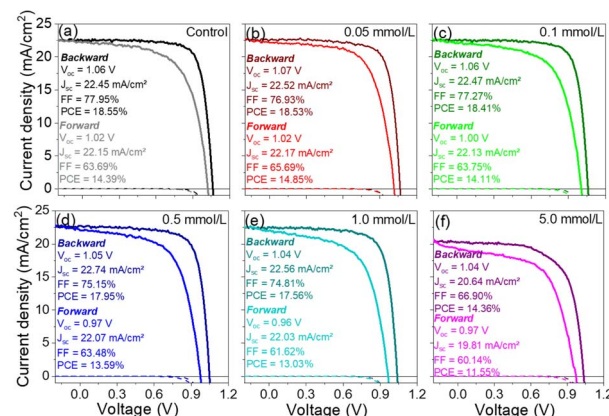

Fig. 6 J–V curves in forward and backward scan directions under illumination (100 mW cm^{-2}) (solid lines) and in the dark (dashed lines) of the best-performing PSCs for each salophen concentration used as an antisolvent: (a) control, (b) 0.05 mmol L^{-1}, (c) 0.1 mmol L^{-1}, (d) 0.5 mmol L^{-1}, (e) 1.0 mmol L^{-1}, and (f) 5.0 mmol L^{-1}.

33180 | J. Mater. Chem. A, 2025, 13, 33175–33187
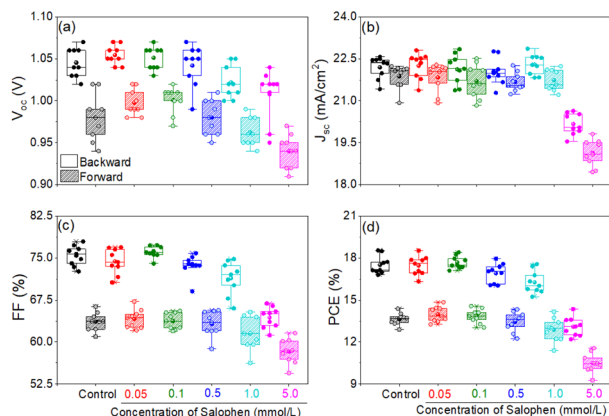
This journal is © The Royal Society of Chemistry 2025

Fig. 7 Statistical distributions of (a) open circuit voltage (V_{oc}), (b) short-circuit current density (J_{sc}), (c) fill factor (FF), and (d) PCE obtained from nine devices for each concentration of salophen (from 0.05 to 5.0 mmol L^{-1}) used as antisolvent for backward and forward scans.

Fig. 7, and their corresponding values are summarized in Table 2.

The statistical distribution results indicate good reproducibility due to the narrow performance deviation between PSCs under the same conditions, as shown in Fig. 7. The photovoltaic parameters of the devices containing 0.05 and 0.1 mmol L^{-1} of salophen on the MAPbI$_3$ layer are comparable with the control PSCs (without salophen), except for the average V_{oc} (forward

scan), which showed a slight improvement from 0.98 ± 0.03 V to 1.00 ± 0.02 V (about 2%, on average). Among the best performance for modified devices, PSCs with salophen-modified MAPbI$_3$ layer at a concentration of 0.1 mmol L^{-1} achieved a maximum average PCE value of $17.69\% \pm 0.45\%$, with a V_{oc} of 1.05 ± 0.01 V, a J_{sc} of 22.13 ± 0.53 mA cm^{-2} and an FF of $76.08\% \pm 1.03\%$ (see Table 2). Comparing the average values, the V_{oc}, FF, and PCE parameters were slightly affected by the increase in salophen concentration (≥ 0.5 mmol L^{-1}) on the perovskite films. For the devices with 5.0 mmol L^{-1} of salophen, the average PCE value decreased sharply to $13.09\% \pm 0.68\%$, with a V_{oc} of 1.01 ± 0.03 V, a J_{sc} of 20.17 ± 0.39 mA cm^{-2} and an FF of $64.38\% \pm 1.91\%$.

The decrease in an FF value can also be attributed mainly to the increase in the sheet resistance value (see Table S1, SI), which reflects the increase in the charge transfer resistance between the MAPbI$_3$ grains, as well as between the perovskite layer and the HTL (Spiro-OMeTAD). The lower performance of PSCs containing higher concentrations (≥ 1.0 mmol L^{-1}) of salophen can be attributed to the excess of chelate molecules, which worsens the MAPbI$_3$ crystallization process, as well as the insulating nature of the Schiff base. In addition, there seems to be no improvement in hysteresis with the use of salophen as an antisolvent compared to the control PSCs (Fig. S4, SI).

In addition, all devices exhibited noticeable hysteresis in the J–V curves, which is typical of mesoporous n–i–p architectures employing MAPbI$_3$ and TiO$_2$. Hysteresis in PSCs has been

Table 2 Photovoltaic parameters of the PSCs with an active area of 0.16 cm^2 measured under illumination (100 mW cm^{-2}) in backward scan (B) and forward scan (F). Average and standard deviation values were obtained based on nine devices. The values in parentheses are for the best-performing PSCs

| Devices | Scans | Experimental | | | | Simulation | | |
		V_{oc} (V)	J_{sc} (mA cm^{-2})	FF (%)	PCE (%)	J_{sc} (mA cm^{-2})	R_s (Ω)	R_{sh} (Ω)
MAPbI$_3$ (control)	B	1.05 ± 0.02 (1.06)	22.20 ± 0.40 (22.45)	75.42 ± 1.80 (77.25)	17.51 ± 0.64 (18.55)	22.36	20.79	6013
	F	0.98 ± 0.03 (1.02)	21.87 ± 0.43 (22.15)	63.64 ± 1.64 (63.69)	13.64 ± 0.44 (14.39)	21.97	21.03	3169
MAPbI$_3$: salophen (0.05 mmol L^{-1})	B	1.05 ± 0.01 (1.07)	22.26 ± 0.46 (22.52)	74.40 ± 2.27 (76.93)	17.46 ± 0.68 (18.53)	22.72	10.31	33 599
	F	1.00 ± 0.02 (1.02)	21.84 ± 0.52 (22.17)	64.13 ± 1.71 (65.69)	13.98 ± 0.54 (14.85)	22.29	14.05	2161
MAPbI$_3$: salophen (0.1 mmol L^{-1})	B	1.05 ± 0.01 (1.06)	22.13 ± 0.53 (22.47)	76.08 ± 1.03 (77.27)	17.69 ± 0.45 (18.41)	22.07	13.98	10 336
	F	1.00 ± 0.02 (1.00)	21.71 ± 0.61 (22.13)	63.74 ± 1.47 (63.75)	13.86 ± 0.51 (14.11)	21.63	15.42	3381
MAPbI$_3$: salophen (0.5 mmol L^{-1})	B	1.04 ± 0.02 (1.05)	22.05 ± 0.47 (22.74)	73.69 ± 1.90 (75.15)	16.93 ± 0.69 (17.95)	22.12	12.37	9866
	F	0.98 ± 0.02 (0.97)	21.68 ± 0.34 (22.07)	63.24 ± 2.29 (63.48)	13.44 ± 0.71 (13.59)	21.59	15.55	2886
MAPbI$_3$: salophen (1.0 mmol L^{-1})	B	1.02 ± 0.02 (1.04)	22.30 ± 0.36 (22.56)	71.44 ± 3.00 (74.81)	16.28 ± 0.81 (17.56)	21.96	12.62	12 244
	F	0.96 ± 0.02 (0.96)	21.74 ± 0.38 (22.03)	61.50 ± 2.98 (61.62)	12.87 ± 0.86 (13.03)	21.33	16.72	2542
MAPbI$_3$: salophen (5.0 mmol L^{-1})	B	1.01 ± 0.03 (1.04)	20.17 ± 0.39 (20.64)	64.38 ± 1.91 (66.90)	13.09 ± 0.68 (14.36)	20.51	13.97	5468
	F	0.94 ± 0.02 (0.97)	19.13 ± 0.48 (19.81)	58.29 ± 2.21 (60.14)	10.49 ± 0.70 (11.55)	19.42	19.64	1090

This journal is © The Royal Society of Chemistry 2025

J. Mater. Chem. A, 2025, **13**, 33175–33187 | **33181**

widely attributed to ionic migration (*e.g.*, I^-, MA^+), trap states at grain boundaries and interfaces, and capacitive effects at the ETL/perovskite and perovskite/HTL interfaces.[69–71] Even when salophen was introduced to passivate surface defects, a significant hysteresis index (HI) persisted across all concentrations, suggesting that the molecular passivation achieved was insufficient to suppress the bulk ionic and capacitive mechanisms. For instance, devices incorporating $MAPbI_3$: salophen at 0.05 and 5.0 mmol L^{-1} showed an approximate 10% reduction in HI relative to the control likely due to partial passivation, but this was not enough to eliminate the interfacial capacitive behaviour. These observations are also in line with studies by Kim and Park, who demonstrated that the meso-TiO_2 morphology and grain boundary density are critical parameters influencing hysteresis magnitude.[69]

To better correlate the experimental data obtained from the PSC devices with some properties of the employed structures, several physical parameters can be estimated, simulating the experimental behaviour with the known equivalent electrical circuit of a solar cell. Typically, such an equivalent electrical circuit attempts to reproduce the device electrical behaviour considering (i) the effect of electrically active defects (parallel resistance R_P), (ii) potential barrier at the electrodes (series resistance R_S), (iii) ideal approximation of the donor–acceptor junction (diode) and (iv) losses in the generation of free excitons (photogenerated current density – J_{PH} – *versus* collected current density – J_{SC}). In this one-diode 'real' solar cell model, the *J–V* data can be given by the following general equation:[72,73]

$$J(V) = J_0\left(\exp\frac{q(V - JR_SA)}{nk_BT} - 1\right) + \frac{V - JR_SA}{R_P} - J_{PH}, \quad (3)$$

where J_0 is the diode saturation current density, q is the electronic charge, n is the diode ideality factor, k_B is the Boltzmann constant, T is the temperature, A is the solar cell active area and V is the voltage. R_S and R_P depend on the device structure and materials. We can consider that J_{PH} (direct photogenerated current density) is voltage independent. Experimental data fitting was performed by employing homemade genetic algorithms searching for the best solution with a minimization of the cost function (error).[74,75] Fig. 8 shows the equivalent electrical circuit and the simulation data for two samples ($MAPbI_3$ control and $MAPbI_3$: salophen 0.05 mmol L^{-1}) in both forward and backward scans. The simulation data for all kinds of solar cells produced are summarized in Table 2.

From the simulated data, we can observe that parallel resistance R_P tends to increase significantly (in backward scan, and compared to the control device) in all salophen-based devices, except for the 5 mmol L^{-1} concentration. The most pronounced increase is observed for the 0.05 mmol L^{-1} concentration, indicating a significantly better molecular conformation with a low density of electrically active defects that can act as traps for the electrical carriers. This observation suggests that for the low incorporation of salophen, we have more free electrical carriers. These results support the aforementioned conclusion that salophen molecules could passivate $MAPbI_3$ defects, promoting a better crystallization domain in the film. In effect, for low salophen concentration, we observe
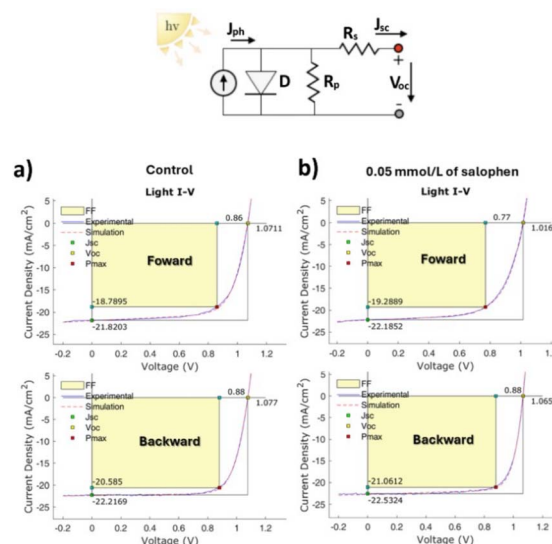

Fig. 8 *J–V* data and simulation of best-performing PSCs for $MAPbI_3$ (control; (a)) and $MAPbI_3$:salophen (0.05 mmol L^{-1}; (b)) in backward and forward scans, according to the solar cell equivalent circuit. The yellow square represents the maximum power, related to the FF.

a better uniformity of grain size (better film uniformization), while for high salophen incorporation, needle-like structures formed between grain boundaries and the surface, which promote a high density of electrically active defects (Fig. S7), are responsible for the low R_P estimated data. Moreover, the relatively low R_P for a salophen concentration of 5 mmol L^{-1} indicates that defect passivation could not be efficient in this sample (in agreement with previous data).

These observations also agree with TrPL decays. Although without any appreciable change in the bandgap, the observed blue shift simultaneously with a decrease in the decay for low salophen concentration (of 0.05 mmoL L^{-1}) indicates a high probability of $MAPbI_3$ defect passivation together with a better crystallization process in the film formation. The relatively small value for R_S reveals that a low potential barrier exists at the electrodes. This observation agrees with the effect that salophen incorporation has on the film (bulk), but there is no evidence of band and/or energy level changes. The high value of R_S for the 5 mmol L^{-1} salophen concentration (and for the control) suggests some charge accumulation in defects localized at interfacial layers at electrodes, but, considering the data, should not be meaningful.

Interestingly, for high salophen incorporation (5.0 mmol L^{-1}), the J_{SC} tends to decrease slightly (compared to the remaining samples) but accompanies a decrease in the estimated J_{PH} values. This should indicate (and following the previous discussion about heterostructure formation at grain boundaries) that such samples have less exciton formation perhaps owing to a decrease in the film absorption as the new heterostructure is formed. In general, J_{SC} and estimated J_{PH} are similar, indicating that almost all exciton formation is collected as free carriers at the electrodes. As a general trend,

33182 | *J. Mater. Chem. A*, 2025, **13**, 33175–33187

This journal is © The Royal Society of Chemistry 2025

photogenerated charge carriers are efficiently extracted by the external circuit, with small non-radiative recombination losses.

The estimated diode ideality factor did not change significantly (around 4 in the forward scan and 2 in the backward scan). This means that the usual model D–A interface exhibits more ideal behaviour in backward scans than in forward ones. A possible explanation can be ascribed to the lesser charge accumulation in the first case and could rely on the usual hysteresis found in PSC devices.

To obtain more insights into the salophen addition in the MAPbI$_3$ thin films and its impact on the non-radiative losses in the PSCs, we estimated the quasi-Fermi level splitting (QFLS) non-radiative V_{oc} variation (ΔV_{OCnRad}), considering the photoluminescence quantum yields (PLQY) of the devices. eqn (4) describes the QFLS dependence on PLQY:[76]

$$QFLS = QFLS_{rad} + k_b T \ln(PLQY), \qquad (4)$$

where QFLS$_{rad}$ is the radiative limit (PLQY = 1) of the device material. In some cases, when there is low interface mismatching between the perovskite film and the ETL and HTL, we can assume at lower intensities (~1 Sun of illumination) that QFLS ~ qV_{oc}, (where q is the elementary charge).[76,77] In our device, the radiative limit is approximately 1.1 eV. Considering these values, the addition of salophen molecules to MAPbI$_3$ thin films reduces the non-radiative losses for the 0.05 mmol L^{-1} condition (PLQY = 0.31) in the backward bias in relation to the control device (PLQY = 0.21) (Fig. S5, SI). However, high concentrations of salophen disturb the interface between MAPbI$_3$ and Spiro-OMeTAD HTL, creating non-radiative pathways, resulting in the decrease of the PLQY and consequently increasing the PSC non-radiative losses. However, the addition of salophen did not change the QFLS under direct bias until 0.5 mmol L^{-1}. Above this concentration, we can observe a behaviour similar to that seen under backward bias.

The stability of these devices under environmental conditions is a major challenge owing to their sensitivity to oxygen and the hygroscopic nature of the perovskite layer.[78] In this context, the stability of the PSCs was evaluated under dark storage conditions by 720 h at room temperature (~25 °C), without any encapsulation, following the ISOS-D-1 protocol.[64] First, the devices were stored in a box with continuous nitrogen flow, maintaining relative humidity from 20% to 22%. Second, the PSCs were exposed to ambient conditions without nitrogen flow, with relative humidity ranging from 55% to 60%. PCE evolution with time for PSCs is shown in Fig. S6 in SI, and normalized PCE data are shown in Fig. 9.

The control PSCs (without salophen) and devices containing salophen-modified MAPbI$_3$ at concentrations of 0.1 mmol L^{-1} and 1.0 mmol L^{-1} did not show significant PCE losses after 720 h in a box with continuous nitrogen flow and with relative humidity between 20% and 22% (see Fig. 9a and b). In fact, PSCs containing a salophen-modified MAPbI$_3$ layer (1.0 mmol L^{-1}) demonstrated the best stability, with a slight gain of 1.2% of the initial PCE value in the backward scan direction and a modest PCE loss of approximately 12% in the forward scan direction.
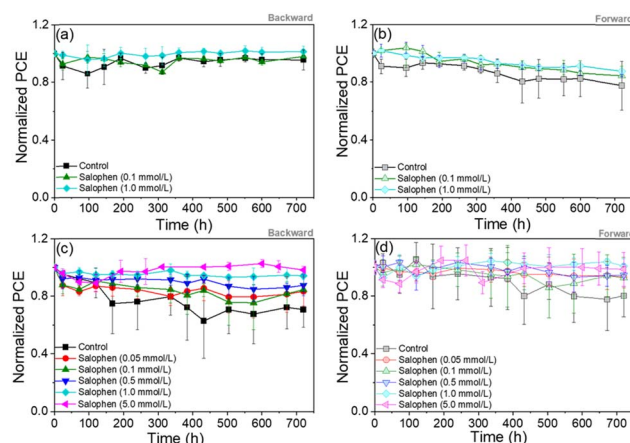

Fig. 9 Normalized PCE evolution of the PSCs stored in the dark under ambient conditions with a relative humidity of (a and b) 20–22% and (c and d) 55–60% without any encapsulation, according to protocol ISOS-D-1, for (a and c) backward and (b and d) forward scans.

As depicted in Fig. 9c and d, PSCs containing salophen at concentrations of 5.0 mmol L^{-1} and 1.0 mmol L^{-1} exhibited the best stabilities under ambient conditions with relative humidity ranging from 55% and 60%, respectively. In the backward scan direction, these devices presented only 1.8% and 5.8% of the initial PCE loss, respectively. In the forward scan, they showed a 1.2% loss and a 1.0% gain in initial PCE loss. The devices with salophen-modified MAPbI$_3$ at concentrations of 0.05 mmol L^{-1}, 0.1 mmol L^{-1} and 0.5 mmol L^{-1} exhibited initial PCE losses of 16.7%, 15.5% and 12.4%, respectively, in the backward scan direction. For the forward scan, the initial PCE losses were 6.6%, 7.2% and 5.3%, respectively. In contrast, initial PCE losses of 29.3% and 19.6% were observed for the PSC used as a control in the backward and forward scans, respectively, after the same period and under the same conditions. The clear improvement in stability may be related to the coordination of the organic ligand (salophen) with the metallic center (Pb^{2+}) of the perovskite through a bond with donor atoms (*e.g.* nitrogen or oxygen).[79,80]
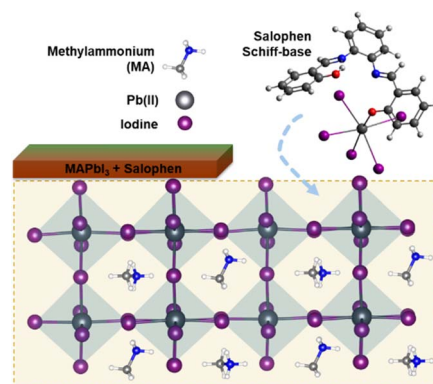

Fig. 10 Illustration of a possible interaction between the salophen molecule and MAPbI$_3$ octahedra and defect passivation possibility.

This journal is © The Royal Society of Chemistry 2025

J. Mater. Chem. A, 2025, **13**, 33175–33187 | **33183**

To better understand the role of salophen in improving the stability and performance of MAPbI$_3$ films, we propose the mechanism illustrated in Fig. 10. Salophen, an N$_2$O$_2$-donor Schiff-base ligand, coordinates undercoordinated Pb^{2+} ions through its imine nitrogen and/or phenolic oxygen atoms. This chelation passivates surface and grain boundary defects (i.e. iodide vacancies – V_I–), suppressing non-radiative recombination pathways. TrPL decays (Fig. 5) confirm this behavior, as charge-carrier lifetimes decrease with salophen addition, indicating more efficient carrier extraction.

Simultaneously, salophen's planar and hydrophobic structure creates a molecular capping layer on the perovskite surface. Contact angle measurements reveal an enhanced water repellent effect, with values increasing from 36.1° (control) to 53.6° (5.0 mmol L^{-1}), confirming improved moisture resistance. This dual action, defect passivation and hydrophobic protection, provides superior environmental stability for salophen-modified PSCs. Devices incorporating salophen at optimal concentrations (0.1–1.0 mmol L^{-1}) exhibited minimal PCE loss under the ISOS-D-1 protocol, even after 720 hours in ambient humidity (55–60%).

Together, these effects demonstrate that salophen acts as a multifunctional additive, improving the crystallization, defect tolerance, and environmental stability of MAPbI$_3$ films processed under ambient conditions.

4 Conclusions

Salophen molecules were dissolved in EA solvent (0.05–5 mmol L^{-1}) and added to MAPbI$_3$ films during antisolvent deposition. X-ray diffraction (XRD) analysis showed enhanced conversion to the black-phase (α-phase) with reduced PbI$_2$ impurities, with subsequent improvement in the film stability under normal ambient conditions (25 °C, ~50% rh) for at least 30 days. Grain size distribution remained unaffected though excess salophen-induced heterostructure formation at grain boundaries, as observed in the FEG-SEM images. Photophysical characterization revealed no disturbance in absorption and photoluminescence (PL), but PL excitation (PLE) confirmed the resonant energy transfer (RET) or charge transfer (CT) processes between each one. Time-resolved PL (TrPL) indicated reduced emission lifetime, better film organization, and fewer structural defects. Salophen-modified PSCs did not present considerable changes in power conversion efficiency compared to the control devices. However, the addition of the salophen chelate molecules into the MAPbI$_3$ devices enhances the global PSC figures of merit (statistical distribution), improving the PCE median values, being the best performance parameter for 0.1 mmol L^{-1} of salophen (PCE = 17.69% ± 0.45%). Concentrations of salophen above 0.1 mmol L^{-1} worsen the features of MAPbI$_3$ solar cells. The data obtained from device physics simulations of the electrical equivalent circuit agree with the PSC structural and photophysical characterizations, confirming defect passivation. Stability tests (ISOS-D-1) showed enhanced durability, with 5 mmol L^{-1} salophen devices maintaining initial PCE for one month (55–60% rh, 25 °C). With these results, new frameworks can be opened for PSC defect passivation towards processable devices under normal environmental conditions.

Author contributions

Conflicts of interest

The authors declare no conflict of interest.

Data availability

The data supporting the findings of this study are available in the manuscript and its SI. See DOI: **https://doi.org/10.1039/d5ta02678d**.

Acknowledgements

33184 | J. Mater. Chem. A, 2025, 13, 33175–33187

This journal is © The Royal Society of Chemistry 2025

References

1 M. Noman, Z. Khan and S. T. Jan, *RSC Adv.*, 2024, **14**, 5085–5131.

2 A. Kojima, K. Teshima, Y. Shirai and T. Miyasaka, *J. Am. Chem. Soc.*, 2009, **131**, 6050–6051.

3 National Renewable Energy Laboratory, *Best Research-Cell Efficiencies*, https://www.nrel.gov/pv/cell-efficiency.html, accessed July 19, 2025.

4 K. A. Bush, K. Frohna, R. Prasanna, R. E. Beal, T. Leijtens, S. A. Swifter and M. D. McGehee, *ACS Energy Lett.*, 2018, **3**, 428–435.

5 D. Meggiolaro, S. G. Motti, E. Mosconi, A. J. Barker, J. Ball, C. Andrea Riccardo Perini, F. Deschler, A. Petrozza and F. De Angelis, *Energy Environ. Sci.*, 2018, **11**, 702–713.

6 J. Kim, S.-H. Lee, J. H. Lee and K.-H. Hong, *J. Phys. Chem. Lett.*, 2014, **5**, 1312–1317.

7 M. Baranowski and P. Plochocka, *Adv. Energy Mater.*, 2020, **10**, 1903659.

8 T. J. Savenije, C. S. Ponseca, L. Kunneman, M. Abdellah, K. Zheng, Y. Tian, Q. Zhu, S. E. Canton, I. G. Scheblykin, T. Pullerits, A. Yartsev and V. Sundström, *J. Phys. Chem. Lett.*, 2014, **5**, 2189–2194.

9 S. De Wolf, J. Holovsky, S.-J. Moon, P. Löper, B. Niesen, M. Ledinsky, F.-J. Haug, J.-H. Yum and C. Ballif, *J. Phys. Chem. Lett.*, 2014, **5**, 1035–1039.

10 V. M. Le Corre, E. A. Duijnstee, O. El Tambouli, J. M. Ball, H. J. Snaith, J. Lim and L. J. A. Koster, *ACS Energy Lett.*, 2021, **6**, 1087–1094.

11 J. Lim, M. T. Hörantner, N. Sakai, J. M. Ball, S. Mahesh, N. K. Noel, Y.-H. Lin, J. B. Patel, D. P. McMeekin, M. B. Johnston, B. Wenger and H. J. Snaith, *Energy Environ. Sci.*, 2019, **12**, 169–176.

12 S. Wieghold, J. Tresback, J.-P. Correa-Baena, N. T. P. Hartono, S. Sun, Z. Liu, M. Layurova, Z. A. VanOrman, A. S. Bieber, J. Thapa, B. Lai, Z. Cai, L. Nienhaus and T. Buonassisi, *Chem. Mater.*, 2019, **31**, 3712–3721.

13 S. D. Stranks, G. E. Eperon, G. Grancini, C. Menelaou, M. J. P. Alcocer, T. Leijtens, L. M. Herz, A. Petrozza and H. J. Snaith, *Science*, 2013, **342**, 341–344.

14 I. M. Asuo, D. Gedamu, N. Y. Doumon, I. Ka, A. Pignolet, S. G. Cloutier and R. Nechache, *Mater. Adv.*, 2020, **1**, 1866–1876.

15 T. Leijtens, K. Bush, R. Cheacharoen, R. Beal, A. Bowring and M. D. McGehee, *J. Mater. Chem. A*, 2017, **5**, 11483–11500.

16 J. Zhuang, J. Wang and F. Yan, *Nano-Micro Lett.*, 2023, **15**, 84.

17 A. A. Sutanto, R. Szostak, N. Drigo, V. I. E. Queloz, P. E. Marchezi, J. C. Germino, H. C. N. Tolentino,

M. K. Nazeeruddin, A. F. Nogueira and G. Grancini, *Nano Lett.*, 2020, **20**, 3992–3998.

18 B. Conings, J. Drijkoningen, N. Gauquelin, A. Babayigit, J. D'Haen, L. D'Oliesleager, A. Ethirajan, J. Verbeeck, J. Manca, E. Mosconi, F. De Angelis and H. Boyen, *Adv. Energy Mater.*, 2015, **5**, 1500477.

19 M. Wang, C. Fei, M. A. Uddin and J. Huang, *Sci. Adv.*, 2022, **8**, eabo5977.

20 S. Cheng and H. Zhong, *J. Phys. Chem. Lett.*, 2022, **13**, 2281–2290.

21 A. Szemjonov, K. Galkowski, M. Anaya, Z. Andaji-Garmaroudi, T. K. Baikie, S. Mackowski, I. D. Baikie, S. D. Stranks and M. S. Islam, *ACS Mater. Lett.*, 2019, **1**, 506–510.

22 H. Jin, E. Debroye, M. Keshavarz, I. G. Scheblykin, M. B. J. Roeffaers, J. Hofkens and J. A. Steele, *Mater. Horiz.*, 2020, **7**, 397–410.

23 M. Dubajic, J. R. Neilson, J. Klarbring, X. Liang, S. A. Bird, K. C. Rule, J. E. Auckett, T. A. Selby, G. Tumen-Ulzii, Y. Lu, Y.-K. Jung, C. Chosy, Y. Zhao, Y. Boeije, M. V. Zimmermann, A. Pusch, L. Gu, X. Jia, Q. Wu, J. C. Trowbridge, E. M. Mozur, A. Minelli, N. Roth, K. W. P. Orr, A. Mahboubi Soufiani, S. Kahmann, I. Kabakova, J. Ding, T. Wu, G. J. Conibeer, S. P. Bremner, M. P. Nielsen, A. Walsh and S. D. Stranks, *Nat. Nanotechnol.*, 2025, **20**, 755–763.

24 K. Frohna, C. Chosy, A. Al-Ashouri, F. Scheler, Y.-H. Chiang, M. Dubajic, J. E. Parker, J. M. Walker, L. Zimmermann, T. A. Selby, Y. Lu, B. Roose, S. Albrecht, M. Anaya and S. D. Stranks, *Nat. Energy*, 2025, **10**, 66–76.

25 K. W. P. Orr, J. Diao, K. Dey, M. Hameed, M. Dubajić, H. L. Gilbert, T. A. Selby, S. J. Zelewski, Y. Han, M. R. Fitzsimmons, B. Roose, P. Li, J. Fan, H. Jiang, J. Briscoe, I. K. Robinson and S. D. Stranks, *ACS Energy Lett.*, 2024, **9**, 3001–3011.

26 J. Hieulle, A. Krishna, A. Boziki, J.-N. Audinot, M. U. Farooq, J. F. Machado, M. Mladenović, H. Phirke, A. Singh, T. Wirtz, A. Tkatchenko, M. Graetzel, A. Hagfeldt and A. Redinger, *Energy Environ. Sci.*, 2024, **17**, 284–295.

27 Y. Zou, W. Yu, H. Guo, Q. Li, X. Li, L. Li, Y. Liu, H. Wang, Z. Tang, S. Yang, Y. Chen, B. Qu, Y. Gao, Z. Chen, S. Wang, D. Zhang, Y. Chen, Q. Chen, S. M. Zakeeruddin, Y. Peng, H. Zhou, Q. Gong, M. Wei, M. Grätzel and L. Xiao, *Science*, 2024, **385**, 161–167.

28 P. Zhang, J. Xiong, W.-H. Chen, P. Du and L. Song, *Dalton Trans.*, 2023, **52**, 15974–15985.

29 B. G. Krishna, D. Sundar Ghosh and S. Tiwari, *Sol. Energy*, 2021, **224**, 1369–1395.

30 H. T. Hussein, R. S. Zamel, M. S. Mohamed and M. K. A. Mohammed, *J. Phys. Chem. Solids*, 2021, **149**, 109792.

31 X. Shi, T. Liu, Y. Dou, X. Hu, Y. Liu, F. Wang, L. Wang, Z. Ren and S. Chen, *Adv. Mater.*, 2024, **36**, 2402785.

32 H. Zhang, L. Pfeifer, S. M. Zakeeruddin, J. Chu and M. Grätzel, *Nat. Rev. Chem.*, 2023, **7**, 632–652.

33 H. Li, C. Zhang, C. Gong, D. Zhang, H. Zhang, Q. Zhuang, X. Yu, S. Gong, X. Chen, J. Yang, X. Li, R. Li, J. Li, J. Zhou,

This journal is © The Royal Society of Chemistry 2025

J. Mater. Chem. A, 2025, **13**, 33175–33187 | **33185**

H. Yang, Q. Lin, J. Chu, M. Grätzel, J. Chen and Z. Zang, *Nat. Energy*, 2023, **8**, 946–955.

34 R. Sharif, A. Khalid, S. W. Ahmad, A. Rehman, H. G. Qutab, H. H. Akhtar, K. Mahmood, S. Afzal and F. Saleem, *Nanoscale Adv.*, 2023, **5**, 3803–3833.

35 J. C. Da Silva, F. L. De Araújo, R. Szostak, P. E. Marchezi, R. F. Moral, J. N. De Freitas and A. F. Nogueira, *J. Mater. Chem. C*, 2020, **8**, 9697–9706.

36 C. Chen, S. Cheng, F. Hu, Z. Su, K. Wang, L. Cheng, J. Chen, Y. Shi, Y. Xia, T. Teng, X. Gao, I. Yavuz, Y. Lou and Z. Wang, *Adv. Mater.*, 2024, **36**, 2403038.

37 D. Yang, R. Yang, K. Wang, C. Wu, X. Zhu, J. Feng, X. Ren, G. Fang, S. Priya and S. Liu, *Nat. Commun.*, 2018, **9**, 3239.

38 Z. Li, B. Li, X. Wu, S. A. Sheppard, S. Zhang, D. Gao, N. J. Long and Z. Zhu, *Science*, 2022, **376**, 416–420.

39 H. Wang, Y. Zheng, G. Zhang, P. Wang, X. Sui, H. Yuan, Y. Shi, G. Zhang, G. Ding, Y. Li, T. Li, S. Yang and Y. Shao, *Adv. Mater.*, 2024, **36**, 2307855.

40 F. Cao, M. Wang and L. Li, *Rev. Mater. Res.*, 2025, **1**, 100020.

41 F. Cao, L. Bian and L. Li, *Energy Materials and Devices*, 2024, **2**, p. 9370018.

42 F. Cao, P. Zhang and L. Li, *Fundam. Res.*, 2022, **2**, 237–253.

43 M. Wang, H. Sun, L. Meng, M. Wang and L. Li, *Adv. Mater.*, 2022, **34**, 2200041.

44 L. Leoni and A. Dalla Cort, *Inorganics*, 2018, **6**, 42.

45 A. Dalla Cort, P. De Bernardin, G. Forte and F. Yafteh Mihan, *Chem. Soc. Rev.*, 2010, **39**, 3863.

46 A. Decortes, A. M. Castilla and A. W. Kleij, *Angew. Chem., Int. Ed.*, 2010, **49**, 9822–9837.

47 I. Pietro Oliveri, S. Failla, A. Colombo, C. Dragonetti, S. Righetto and S. Di Bella, *Dalton Trans.*, 2014, **43**, 2168–2175.

48 D. Baecker, Ö. Sesli, L. Knabl, S. Huber, D. Orth-Höller and R. Gust, *Eur. J. Med. Chem.*, 2021, **209**, 112907.

49 J. Zhang, F. Zhao, X. Zhu, W.-K. Wong, D. Ma and W.-Y. Wong, *J. Mater. Chem.*, 2012, **22**, 16448.

50 M. G. Vivas, J. C. Germino, C. A. Barboza, P. A. M. Vazquez, L. De Boni, T. D. Z. Atvars and C. R. Mendonça, *J. Phys. Chem. C*, 2016, **120**, 4032–4039.

51 M. G. Vivas, J. C. Germino, C. A. Barboza, D. de A. Simoni, P. A. M. Vazquez, L. De Boni, T. D. Z. Atvars and C. R. Mendonça, *J. Phys. Chem. C*, 2017, **121**, 1283–1290.

52 M. G. Vivas, C. A. Barboza, J. C. Germino, R. D. Fonseca, D. L. Silva, P. A. M. Vazquez, T. D. Z. Atvars, C. R. Mendonça and L. De Boni, *J. Phys. Chem. A*, 2021, **125**, 99–105.

53 L. G. T. A. Duarte, J. C. Germino, R. A. Mendes, J. F. Berbigier, M. M. Faleiros, F. S. Rodembusch and T. D. Z. Atvars, *Dyes Pigm.*, 2019, **171**, 107671.

54 L. G. T. A. Duarte, J. C. Germino, R. A. Mendes, J. F. Berbigier, K. S. Moreira, M. M. Faleiros, J. N. De Freitas, T. A. L. Burgo, F. S. Rodembusch and T. D. Z. Atvars, *J. Phys. Chem. C*, 2020, **124**, 21036–21046.

55 L. G. T. A. Duarte, J. C. Germino, J. F. Berbigier, C. A. Barboza, M. M. Faleiros, D. de Alencar Simoni, M. T. Galante, M. S. de Holanda, F. S. Rodembusch and T. D. Z. Atvars, *Phys. Chem. Chem. Phys.*, 2019, **21**, 1172–1182.

56 E. S. Moraes, L. G. Teixeira Alves Duarte, J. C. Germino and T. D. Z. Atvars, *J. Phys. Chem. C*, 2020, **124**, 22406–22415.

57 J. C. Germino, J. N. de Freitas, R. A. Domingues, F. J. Quites, M. M. Faleiros and T. D. Z. Atvars, *Synth. Met.*, 2018, **241**, 7–16.

58 E. S. Moraes, L. G. T. A. Duarte, F. S. Rodembusch, J. C. Germino, L. F. R. Pereira and T. D. Z. Atvars, *Mater. Adv.*, 2024, **5**, 7778–7788.

59 C. A. Barboza, J. C. Germino, A. M. Santana, F. J. Quites, P. A. M. Vazquez and T. D. Z. Atvars, *J. Phys. Chem. C*, 2015, **119**, 6152–6163.

60 J. C. Germino, J. N. de Freitas, R. A. Domingues, F. J. Quites, M. M. Faleiros and T. D. Z. Atvars, *Synth. Met.*, 2018, **241**, 7–16.

61 C. Che, C. Kwok, S. Lai, A. F. Rausch, W. J. Finkenzeller, N. Zhu and H. Yersin, *Chem.–Eur. J.*, 2010, **16**, 233–247.

62 J. C. Germino, L. G. T. A. Duarte, R. A. Mendes, M. M. Faleiros, A. de Morais, J. N. de Freitas, L. Pereira and T. D. Z. Atvars, *Nanomaterials*, 2022, **12**, 2497.

63 M. Saliba, J. P. Correa-Baena, C. M. Wolff, M. Stolterfoht, N. Phung, S. Albrecht, D. Neher and A. Abate, *Chem. Mater.*, 2018, **30**, 4193–4201.

64 M. V. Khenkin, E. A. Katz, A. Abate, G. Bardizza, J. J. Berry, C. Brabec, F. Brunetti, V. Bulović, Q. Burlingame, A. Di Carlo, R. Cheacharoen, Y. B. Cheng, A. Colsmann, S. Cros, K. Domanski, M. Dusza, C. J. Fell, S. R. Forrest, Y. Galagan, D. Di Girolamo, M. Grätzel, A. Hagfeldt, E. von Hauff, H. Hoppe, J. Kettle, H. Köbler, M. S. Leite, S. (Frank) Liu, Y. L. Loo, J. M. Luther, C. Q. Ma, M. Madsen, M. Manceau, M. Matheron, M. McGehee, R. Meitzner, M. K. Nazeeruddin, A. F. Nogueira, Ç. Odabaşı, A. Osherov, N. G. Park, M. O. Reese, F. De Rossi, M. Saliba, U. S. Schubert, H. J. Snaith, S. D. Stranks, W. Tress, P. A. Troshin, V. Turkovic, S. Veenstra, I. Visoly-Fisher, A. Walsh, T. Watson, H. Xie, R. Yıldırım, S. M. Zakeeruddin, K. Zhu and M. Lira-Cantu, *Nat. Energy*, 2020, **5**, 35–49.

65 R. Szostak, J. A. P. Castro, A. S. Marques and A. F. Nogueira, *J. Photonics Energy*, 2017, **7**, 022002.

66 T. J. Jacobsson, J.-P. Correa-Baena, E. Halvani Anaraki, B. Philippe, S. D. Stranks, M. E. F. Bouduban, W. Tress, K. Schenk, J. Teuscher, J.-E. Moser, H. Rensmo and A. Hagfeldt, *J. Am. Chem. Soc.*, 2016, **138**, 10331–10343.

67 M. B. Johnston and L. M. Herz, *Acc. Chem. Res.*, 2016, **49**, 146–154.

68 D. W. deQuilettes, K. Frohna, D. Emin, T. Kirchartz, V. Bulovic, D. S. Ginger and S. D. Stranks, *Chem. Rev.*, 2019, **119**, 11007–11019.

69 H. S. Kim and N. G. Park, *J. Phys. Chem. Lett.*, 2014, **5**, 2927–2934.

70 D. Kang and N. Park, *Adv. Mater.*, 2019, **31**, 1805214.

71 R. Singh and M. Parashar, in *Soft-Matter Thin Film Solar Cells*, AIP Publishing LLCMelville, New York, 2021, pp. 1–42.

72 S. M. Sze and K. K. Ng, in *Physics of Semiconductor Devices*, Wiley, 2006.

33186 | *J. Mater. Chem. A*, 2025, **13**, 33175–33187

This journal is © The Royal Society of Chemistry 2025

73 M. A. Green, in *Solar Cells: Operating Principles, Technology and System Applications*, Prentice-Hall, Englewood Cliffs, 1982.

74 A. J. Trindade and L. Pereira, *Int. J. Photoenergy*, 2017, **2017**, 1–10.

75 A. J. Trindade, M. G. Santos, J. Gomes and L. Pereira, *MRS Proc.*, 2011, **1359**, 619.

76 P. Caprioglio, M. Stolterfoht, C. M. Wolff, T. Unold, B. Rech, S. Albrecht and D. Neher, *Adv. Energy Mater.*, 2019, **9**, 1901631.

77 J. Warby, S. Shah, J. Thiesbrummel, E. Gutierrez-Partida, H. Lai, B. Alebachew, M. Grischek, F. Yang, F. Lang, S. Albrecht, F. Fu, D. Neher and M. Stolterfoht, *Adv. Energy Mater.*, 2023, **13**, 2303135.

78 P. E. Marchezi, E. M. Therézio, R. Szostak, H. C. Loureiro, K. Bruening, A. Gold-Parker, M. A. Melo, C. J. Tassone, H. C. N. Tolentino, M. F. Toney and A. F. Nogueira, *J. Mater. Chem. A*, 2020, **8**, 9302–9312.

79 S. K. Seth, A. Bauzá, G. Mahmoudi, V. Stilinović, E. López-Torres, G. Zaragoza, A. D. Keramidas and A. Frontera, *CrystEngComm*, 2018, **20**, 5033–5044.

80 O. Yaffe, Y. Guo, L. Z. Tan, D. A. Egger, T. Hull, C. C. Stoumpos, F. Zheng, T. F. Heinz, L. Kronik, M. G. Kanatzidis, J. S. Owen, A. M. Rappe, M. A. Pimenta and L. E. Brus, *Phys. Rev. Lett.*, 2017, **118**, 136001.

This journal is © The Royal Society of Chemistry 2025

J. Mater. Chem. A, 2025, **13**, 33175–33187 | **33187**